FINITE ELEMENT ANALYSIS OF HYPERELASTOPLASTIC MIXED-HARDENING MATERIALS UNDER PLANE STRESSES

J. P. Pascon

A finite element formulation for the analysis of elastoplastic materials under finite strain levels, plane stress conditions, and mixed hardening is developed. The 3D hyperelastoplastic framework is condensed into a compact 2D form following the plane stress condition. The constitutive modeling accounts for the finite elastoplastic strains, associative plasticity, and mixed hardening. A kinematical approximation is based on the positional description and the isoparametric triangular membrane element of any order. Some examples are used to test the numerical formulation proposed. Several meshes are employed for each problem, varying the number of elements and approximation degree, which increases up to the fourth order. The results show that mesh refinement improves accuracy, avoiding locking problems and hourglass instabilities in plane stress problems involving large elastoplastic deformation, stress concentration, bending, mesh distortion, and post-buckling behavior. In addition to the convergence analysis regarding displacements and forces, some final values of the isotropic hardening parameter, the equivalent stress, and the backstress components are provided in order to assess the performance of all the element orders more completely. A comparison of the present results with finite element solutions from the scientific literature available is done, highlighting the similarities and differences for each problem.

Keywords: hyperelastoplasticity, plane stress condition, large deformation analysis, 2D triangular finite elements

1. Introduction. The development of large strain elastoplastic models for plane stress conditions remains a major challenge. Most constitutive laws are defined within the context of a three-dimensional framework, but model calibration usually involves material testing in plane stress conditions. In general, plane stress versions of elastoplastic models are difficult or even impossible to be obtained, especially for large strain regime. This procedure is not straightforward, as in the case of linear elastic materials under small strains, since the expressions involved are highly nonlinear.

In large strain regime, a widely accepted 3D framework for elastoplastic materials is the hyperelastoplasticity, in which the deformation gradient is multiplicatively decomposed into elastic and plastic parts, and the stresses are derived from a strain energy density function. Several hyperelastoplastic models have been proposed in the scientific literature for isotropic materials under isothermal conditions (see, e.g., [10, 34, 38, 43, 44]). Examples of anisotropic hyperelastoplastic formulations can be found in [12, 24, 25], and thermo-mechanical models for elastomers have been proposed in [14–16], among others. In addition, coupling with fracture analysis is performed, for example, in [2–4]. For rate-dependent models in large-strain elastoplastic regime, one can cite [1, 21, 22, 26, 46].

Even in the simplest case of J_2 flow theory (associative Von Mises plasticity), the imposition of plane stress conditions leads to additional nonlinear equations involving tensor quantities. The inclusion of isotropic and kinematic hardening behavior further increases the mathematical complexity of the modeling. Some numerical strategies have been proposed to condense

general 3D models regarding plane stress conditions. In [37], for example, a finite element formulation is developed for elastoplastic analysis of plane membrane problems. A quadrilateral element with four nodes and one layer integration is employed by those authors to guarantee that the out-of-plane shearing stresses are null. The remaining plane stress constraint ($\sigma_{33} = 0$) is satisfied in a weak sense considering the thickness variation as a weighting function. Another interesting procedure has been presented by [19], in which physically nonlinear 3D models are incorporated in beam and shell finite elements. To this end, the condensation with respect to the zero-stress condition is performed by the local algorithm developed. The advantage of both formulations is that arbitrary 3D constitutive laws can be employed for plane stress analysis without any specific modification in the material model, avoiding static condensation. The disadvantage, in turn, is that all the 3D stress components, as well as the complete consistent tangent operator, must be determined. In the context of finite element analysis, for example, this leads to a higher computational effort in terms of processing time and memory capacity. In this paper, explicit plane stress compact forms of an isotropic hyperelastoplastic model including mixed hardening are originally developed. Therefore, the stress tensor is represented by a 2×2 matrix and the consistent tangent operator is a $2 \times 2 \times 2 \times 2$ fourth order tensor, avoiding the use of unnecessary computer memory usage. The present Lagrangian model is based on the right Cauchy-Green stretch tensor and on the second Piola-Kirchhoff stress tensor. A similar plane stress Eulerian model has been presented in [18], which the Kirchhoff stress tensor, the logarithmic stretches and the left Cauchy-Green stretch tensor are employed. In the plane stress formulations of [18, 19, 37], however, only isotropic hardening is considered.

Many finite element approaches have been proposed over the last decades to solve plane problems involving highly deformable elastoplastic materials. It is well known that low order standard (pure-displacement based) formulations exhibit severe stiffening (or locking) behavior in bending and incompressible problems. Several alternative techniques have been developed to improve the performance of low order elements in plane elastoplastic problems. In the present context, one can cite the following quadrilateral finite element formulations, among many others: the mixed three-field formulation of [33], which focus on the treatment of the incompressibility constraint; the reduced integration method proposed in [36], in which a one-point integration scheme is employed to solve volumetric locking in near-incompressible problems and, thus, a hourglass stabilization procedure is needed; the modified enhanced strain method of [13], proposed to remove hourglass modes in elements under inelastic deformations; the mixed formulation of [5] employed to develop two new elements, in which the deformation gradient is included as an additional variable, leading to a fourth field functional; and the element formulation of [35] based on the assumed strain method, in which an updated Lagrangian framework is developed for large deformation sensitivity analysis. These alternative formulations are usually very complicated and case-dependent. A more natural and simplified way of solving locking problems is by using high order elements. Some authors argue that high order elements are more sensitive to mesh distortions [5]. This is probably due to the fact that, in finite deformation problems, the element Jacobian (which is a measure of volumetric strain) tends to be sensitive to large deformation levels [33] and, thus, may become negative, leading to an unrealistic material response. For the present author, however, high order elements provide more accurate results and a locking-free behavior, leading to a robust and, at the same time, simple formulation. Examples of high order elements successfully employed in large deformation analysis can be found in [28, 29, 31], which solid tetrahedral, shell and beam elements based on positional description are used, respectively. It is demonstrated, in such works, that the use of high order elements fully integrated avoids locking problems for sufficiently refined meshes. The superior performance of high order elements is also shown by the so-called p-version of the Finite Element Method (FEM), in which the polynomial degree of the elements is increased until convergence is achieved [11, 17, 41, 42]. As pointed out in [41], the spurious stress oscillations are alleviated if the polynomial order is sufficiently high. The only shortcoming of this procedure is the large computational effort, which can be circumvented by high performance computing (or parallel-processing techniques). A novel feature of the present work is the original investigation of the performance of triangular finite elements of various orders in the context of plane stress hyperelastoplasticity with mixed hardening. In most numerical studies in the context of the FEM, only one (or two at the most) approximation order is used to assess the element performance, even in the cases of comparison among different formulations.

The purpose of this study is to condense a large strain elastoplastic model with mixed hardening according to plane stress conditions, as well as to assess the performance of various element orders. The proposed formulation is tested in structural problems involving large displacements and finite levels of elastic and plastic strains.

The paper is organized as follows. The plane stress condensation from the 3D hyperelastoplastic framework is fully detailed in Sec. 2. The finite element adopted and the numerical algorithm implemented in a computer code are described in Sec. 3. The numerical examples used to assess the proposed formulation are provided in Sec. 4. Finally, the main conclusions based on the results are given in Sec. 5.

2. Constitutive Modeling. The 3D hyperelastoplastic framework is described in this section, covering the finite-strain kinematics, the stress-strain response, the yield criterion and the evolution equations, together with further details about the plane stress condensation. The present isotropic model accounts for large elastoplastic strains and nonlinear isotropic and kinematic hardening rules. The derivation of the complete 3D model can be found in [10] and [43].

2.1. Kinematics. The body is assumed to lie on the plane $x_1 - x_2$ at the initial (undeformed) configuration or, equivalently, on the plane $y_1 - y_2$ at the final (deformed) position. The constitutive model is based on the Kröner-Lee decomposition, usually employed in large elastoplastic models (see, e.g., [10, 12, 38, 43], among many others):

$$F = F_e F_p, \tag{2.1}$$

where F is the deformation gradient; and the subscripts e and p denote the elastic and plastic parts, respectively. This decomposition leads to the definition of a local intermediate configuration $F = F_p$, which is stress-free (or relaxed).

The strain measure adopted is the symmetric right Cauchy-Green stretch tensor, which can be decomposed from (2.1) as follows:

$$C = F^T F = F_p^T C_e F_p \Rightarrow C_e = F_p^{-T} C F_p^{-1}. \tag{2.2}$$

Due to the plane stress condition, the tensor C has the following matrix representation (the same is valid for the gradient F):

$$C = \begin{bmatrix} C_{11} & C_{12} & 0 \\ C_{21} & C_{22} & 0 \\ 0 & 0 & C_{33} \end{bmatrix}. \tag{2.3}$$

For the plane strain assumption, one must set $C_{33} = 1$. In the plane stress case, the entry C_{33} is an implicit function of the plane components C_{11}, C_{12}, and C_{22}, which are directly determined from the kinematical approximation adopted (see Sec. 3.1).

In the present study, the elastic material response is described in terms of the elastic Cauchy–Green stretch tensor C_e (see expression 2.2). Under the assumption of isotropy, the following strain invariants are employed:

$$i_{e1} = \mathrm{tr}\, C_e = \mathrm{tr}(F_p^{-T} C F_p^{-1}) = C : C_p^{-1}, \tag{2.4}$$

$$i_{e3} = \det C_e = \det(F_p^{-T} C F_p^{-1}) = \frac{\det C}{\det C_p} = \frac{J^2}{J_p^2}, \tag{2.5}$$

where $J = \det F = \sqrt{\det C}$ is the Jacobian, which is a measure of volumetric strain denoting the local ratio between infinitesimal volume elements defined in the current and initial configurations ($J = (dv)/(dV_0)$); and C_p is the plastic Cauchy–Green stretch. It may be noted that the determination of the plastic gradient F_p and the elastic stretch tensor C_e are not needed, since the strain invariants (2.4) and (2.5) can be calculated directly from the stretch tensors C and C_p. This fact provides two advantages: from a theoretical point of view, unlike the right Cauchy-Green stretch tensor, the gradient is not an objective strain measure; and, regarding computer implementation, since the stretch tensor is symmetric, there are fewer independent components to be determined and stored.

2.2. Stress. The stress and backstress measures are described in this subsection, including the hyperelastic response and condensation according to the plane-stress conditions.

As in hyperelasticity, the stresses can be obtained in hyperelastoplastic models from the Helmholtz free-energy function. In this paper, this scalar strain-energy density function is additively decomposed:

$$\psi = \psi_e(C, C_p) + \psi_p(C_p, q) \quad \text{or} \quad \psi = \psi_e(C_e) + \psi_p(C_p, q), \tag{2.6}$$

where q is a general vector representing hardening parameters. As pointed out in [30], the general form (2.6) presents two properties: elastic material isomorphism [38], as the reversible material response is not changed by dissipative parameters (C_p and q); and rate-independence, since the material response is not influenced by the strain rate ($\dot{C}$). Applying the second law of thermodynamics and the Coleman–Noll procedure to (2.6), it is possible to show that [8]:

$$S_e = 2\frac{\partial \psi_e}{C_e}, \tag{2.7}$$

$$d_{\text{int}} = (M_e - \chi) : D_p - \left(\frac{\partial \psi_p}{\partial q}\right) : \dot{q} \geq 0, \tag{2.8}$$

where S_e is the elastic second Piola–Kirchhoff stress tensor; d_{int} is the internal dissipation; $M_e = C_e S_e$ is the elastic Mandel stress tensor; χ is the intermediate backstress tensor (related to kinematic hardening); and D_p is the plastic strain rate. These tensors are defined at the intermediate configuration. The evolution equations for the rates D_p and $\dot{q}$ are provided in Sec. 2.4.

The hyperelastic model adopted to describe the finite strain elastic response is the compressible Neo–Hookean law (see, e.g., [40]):

$$\psi_e(C_e) = \frac{K}{2}[\ln J_e]^2 + \frac{\mu}{2}\left[i_{e1} - 3 - 2\ln(J_e)\right], \tag{2.9}$$

where K and μ are the bulk and shear moduli, respectively. Such isotropic hyperelastic model is usually employed for elastomers under finite elastic strains. Combining (2.7) and (2.9), the hyperelastic stress-strain model is obtained:

$$S_e = K\ln(J_e)C_e^{-1} + \mu(I - C_e^{-1}), \tag{2.10}$$

where I is the identity matrix. If plastic deformation occurs ($C_p \neq I$), the (total) second Piola–Kirchhoff stress tensor defined at the reference (undeformed) configuration can be derived in a similar way:

$$S = 2\frac{\partial \psi}{\partial C} = F_p^{-1}\left(2\frac{\partial \psi_e}{\partial C_e}\right)F_p^{-T} = F_p^{-1}S_e F_p^{-T}. \tag{2.11}$$

As one can note, the stress tensor S represents the pull-back operation on S_e via F_p. In other words, the stress S_e is brought back (or transferred) to the reference configuration. Similarly, the backstress tensor in (2.8) can also be set in the reference configuration via a pull-back operation:

$$\chi = F_p\left(2\frac{\partial \psi_p}{\partial C_p}\right)F_p^T = F_p X F_p^T \quad \text{or} \quad X = F_p^{-1}\chi F_p^{-T}. \tag{2.12}$$

It should be pointed out that the backstress tensors are defined from the evolution equations provided in Sec. 2.4 and, thus, the explicit form of ψ_p is not needed. One can find explicit expressions for ψ_p in [10] and [43], in which the internal dissipation inequality (2.8) is shown to be satisfied.

The true Cauchy stress tensor at the current configuration can be determined with the usual expression:

$$\sigma = \frac{1}{J}FSF^T. \tag{2.13}$$

Since all the gradients (F, F_e, and F_p) and all the stretch tensors (C, C_e, and C_p) have the matrix form (2.3), the zero-stress condition for the out-of-plane shear components (with indices 13, 23, 31 and 32) is automatically satisfied. Moreover, the remaining plane stress condition can be expressed by the following equivalent equalities:

$$\sigma_{33} = S_{33} = M_{e33} = S_{e33} = 0. \tag{2.14}$$

As performed in [18] for the Kirchhoff stress tensor, the combination of expression (2.10) with the last equality in (2.14) leads to:

$$S_{e33} = K\ln(J_e)\frac{1}{C_{e33}} + \mu\left(1 - \frac{1}{C_{e33}}\right) = 0 \Rightarrow K\ln(J_e) = \mu(1 - C_{e33}). \tag{2.15}$$

Applying the above result to expression (2.10), one obtains the compact plane stress equation for the elastic stress tensor:

$$S_e = \mu(I - C_{e33}C_e^{-1}).$$ (2.16)

The stress tensor S is finally obtained from expressions (2.11) and (2.16):

$$S = \mu F_p^{-1}(I - C_{e33}C_e^{-1})F_p^{-T} = \mu(C_p^{-1} - C_{e33}C^{-1}) = \mu\left(C_p^{-1} - \frac{C_{33}}{C_{p33}}C^{-1}\right).$$ (2.17)

The same result would be obtained if the condition $S_{33} = 0$ were directly applied to (2.11). One should highlight that all the plane stress components S_{11}, S_{12}, and S_{22} can be obtained from stretch tensors C and C_p. As in the case of the elastic strain invariants (2.4) and (2.5), determination of the plastic gradient F_p is not needed. In addition, similarly to [18], the out-of-plane normal stretch C_{33} can be obtained iteratively from (2.15); see Sec. 3.1. The plastic entry C_{p33}, in turn, is obtained from the plane plastic stretch components C_{p11}, C_{p12}, and C_{p22} applying the evolution equation adopted (see Sec. 2.4). Therefore, all the plane stresses can be calculated from the plane stretch components.

2.3. Yield Criterion and Hardening. The yield criterion is set by applying the von Mises yield function to the elastic Mandel stress and to the intermediate backstress:

$$\phi = ||\mathrm{dev}(M_e - \chi)|| - \sqrt{\frac{2}{3}}\sigma_\kappa \leq 0,$$ (2.18)

where ϕ is the yield function; $\mathrm{dev}(\ )$ is the deviatoric operator; and σ_κ is the yield stress, which is a function of the isotropic hardening parameter κ (see Sec. 2.4). As demonstrated in [10], the yield criterion (2.18) can be alternatively expressed in the reference configuration:

$$\phi = ||\mathrm{dev}(CS - C_pX)|| - \sqrt{\frac{2}{3}}\sigma_\kappa \leq 0.$$ (2.19)

The Lagrangian tensor $Y = CS - C_pX$ also has the matrix representation (2.3) and, in general, is non-symmetric. The general vector q in (2.8) contains the isotropic hardening parameter κ and the backstress tensor (χ or X), which is related to kinematic hardening. Two isotropic hardening rules are adopted in the present paper:

$$\sigma_\kappa = Y_s(\varepsilon_0 + \kappa)^n,$$ (2.20)

$$\sigma_\kappa = Y_0 + (Y_{sat} - Y_0)(1 - \exp^{-\beta\kappa}) + H\kappa,$$ (2.21)

where Y_S, ε_0, and n are the coefficients of the Swift model [39]; and Y_0, Y_{sat}, β, and H are the coefficients of the Voce model [45]. Both models are usually employed to describe the isotropic hardening behavior of metals, such as steel and aluminum alloys. The kinematic hardening rule, in turn, is described in rate form (see Sec. 2.4).

2.4. Evolution Equations. The model is completed by setting the flow rule, as well as the rate of the isotropic hardening parameter and the backstress tensor. As in [10] and [43], the following evolution equations have been selected to fulfill the internal dissipation inequality (2.8):

$$D_p = \dot{\gamma}R_p = \dot{\gamma}\frac{\partial\phi}{\partial M_e} = \dot{\gamma}\frac{\mathrm{dev}(M_e - \chi)}{||\mathrm{dev}(M_e - \chi)||} = \dot{\gamma}F_p^{-T}\frac{\mathrm{dev}Y}{||\mathrm{dev}Y||}F_p^T,$$ (2.22)

$$\dot{\kappa} = \dot{\gamma}r_\kappa = \dot{\gamma}\sqrt{2/3}||R_p||,$$ (2.23)

$$\overset{\circ}{\chi} = c\dot{D}_p - \dot{\gamma}b\chi = \dot{\gamma}\overset{\bullet}{R}_\chi = \dot{\gamma}(cR_p - b\chi),$$ (2.24)

where $\dot{\gamma} \geq 0$ is the plastic multiplier, which satisfies the consistency condition $\dot{\gamma}\phi = 0$, $\boldsymbol{R}_p$ and $\boldsymbol{R}_\chi$ denote, in this order, the tensors that describe the "direction" of the plastic flow and the backstress tensor; r_κ is the scalar function that represents the evolution of the isotropic hardening parameter; and the coefficients c and b define the nonlinear Armstrong-Frederick kinematic hardening model. If one sets $b = 0$, model (2.24) will correspond to the Prager kinematic hardening rule. As pointed out in [10], the Armstrong-Frederick rule is more adequate for metals compared to the Prager model, since it can reproduce the Bauschinger and the ratchetting effects.

Expression (2.22) represents the associative plastic flow rule, which is commonly adopted in elastoplastic models. Because of the deviatoric character of tensor $\boldsymbol{R}_p$, the evolution equation (2.23) can be replaced by $\dot{\kappa} = \dot{\gamma}r_\kappa = \dot{\gamma}\sqrt{2/3}$. In this case, parameter κ is also called equivalent plastic strain. A Lagrangian version of the flow rule (2.22), which is needed in the present work, can be obtained from the relation between $\boldsymbol{D}_p$ and the rate of $\boldsymbol{C}_p$:

$$\dot{\boldsymbol{C}}_p = 2\boldsymbol{F}_p^T \boldsymbol{D}_p \boldsymbol{F}_p = 2\dot{\gamma}\,\boldsymbol{F}_p^T \boldsymbol{R}_p \boldsymbol{F}_p = \dot{\gamma}\,\boldsymbol{R}_{cp} = 2\dot{\gamma}\,\frac{\mathrm{dev}\,\boldsymbol{Y}}{||\mathrm{dev}\,\boldsymbol{Y}||}\boldsymbol{C}_p, \tag{2.25}$$

where $\boldsymbol{R}_{cp}$ is the tensor that set the "direction" of the rate of $\boldsymbol{C}_p$.

It can be demonstrated that the associative flow rule (2.22) or (2.25) leads to the plastic incompressibility condition:

$$\frac{d}{dt}(J_p^2) = \frac{\partial J_p^2}{\partial \boldsymbol{C}_p}:\dot{\boldsymbol{C}}_p = J_p^2 \boldsymbol{C}_p^{-1}:\left(2\dot{\gamma}\,\frac{\mathrm{dev}\,\boldsymbol{Y}}{||\mathrm{dev}\,\boldsymbol{Y}||}\boldsymbol{C}_p\right) = 2J_p^2\,\dot{\gamma}\,\mathrm{tr}\left(\frac{\mathrm{dev}\,\boldsymbol{Y}}{||\mathrm{dev}\,\boldsymbol{Y}||}\right) = 0. \tag{2.26}$$

If the rate of the plastic Jacobian is zero, then:

$$J_p^2 = 1 \Rightarrow (C_{p11}C_{p22} - C_{p12}^2)C_{p33} = 1 \Rightarrow C_{p33} = \frac{1}{C_{p11}C_{p22} - C_{p12}^2}. \tag{2.27}$$

As mentioned in Sec. 2.2, the out-of-plane plastic stretch C_{p33} can be determined directly from the plane plastic stretches.

The reason of adopting the objective rate in (2.24) is that the backstress tensor $\boldsymbol{\chi}$ is defined at the intermediate configuration and, thus, the time derivative $\dot{\boldsymbol{\chi}}$ is not objective. Using the objective Jaumann rate, [10] showed the following result:

$$\overset{\circ}{\boldsymbol{\chi}} = \dot{\boldsymbol{\chi}} - \boldsymbol{W}_p \boldsymbol{\chi} + \boldsymbol{\chi}\boldsymbol{W}_p = \boldsymbol{F}_p\left[\dot{\boldsymbol{X}} + \mathrm{sym}(\boldsymbol{C}_p^{-1}\dot{\boldsymbol{C}}_p\,\boldsymbol{X})\right]\boldsymbol{F}_p^T, \tag{2.28}$$

where $\boldsymbol{W}_p$ is the plastic spin rate; and $\mathrm{sym}(\ )$ denotes the symmetric part of a second-order tensor. Combining expressions (2.24), (2.25) and (2.28), the following evolution equation for the initial backstress tensor can be obtained:

$$\dot{\boldsymbol{X}} = \dot{\gamma}\,\boldsymbol{R}_X = \dot{\gamma}\left[c\boldsymbol{C}_p^{-1}\frac{\mathrm{dev}\,\boldsymbol{Y}}{||\mathrm{dev}\,\boldsymbol{Y}||} - b\boldsymbol{X} - \mathrm{sym}\left(2\boldsymbol{C}_p^{-1}\frac{\mathrm{dev}\,\boldsymbol{Y}}{||\mathrm{dev}\,\boldsymbol{Y}||}\boldsymbol{C}_p \boldsymbol{X}\right)\right]. \tag{2.29}$$

One can note that the evolution tensors $\boldsymbol{R}_{cp}$ and $\boldsymbol{R}_X$ are completely defined by Lagrangian measures ($\boldsymbol{C}, \boldsymbol{C}_p$, and $\boldsymbol{X}$), avoiding the use of objective rates. Moreover, these tensors have the matrix representation (2.3). Another issue to be pointed out is that the plastic potential ψ_p, which appears in expression (2.6), depends on objective measures ($\boldsymbol{C}_p$, κ, and $\boldsymbol{X}$) and, thus, it is also objective (or frame-invariant).

3. Numerical Algorithm. The kinematic finite element approximation and the numerical procedures implemented are described in this section. The dual-phase strategy encompassing the elastic predictor and the plastic update is also provided, together with the hyperelastoplastic consistent tangent operator.

3.1. Finite Element. The finite element adopted is the isoparametric triangular membrane of any-order based on positional description. As in the kinematic modeling of Sec. 2.1, the element mid-surface can move only along the plane and,

because of the plane stress condition, the transverse (out-of-plane) normal strain is constant thought the thickness direction, leading to a linearly variable transverse displacement.

The numerical approximation is based on the positional version of the finite element method (FEM) described, for example, in [6, 7, 29]. Both initial and current configurations defined, respectively, by the positional vector fields $\boldsymbol{x}$ and $\boldsymbol{y}$ are mapped from an auxiliary non-dimensional triangular plane, represented by the set $\{(\xi_1, \xi_2) \in R^2 / 0 \leq \xi_1, \xi_2, \xi_1 + \xi_2 \leq 1\}$. The nodes at this plane are equidistant for any order of approximation. The plane vector fields $\boldsymbol{x}$ and $\boldsymbol{y}$ are interpolated via the usual procedure, that is, from nodal positions and shape functions:

$$x = X^k \phi_k(\xi), \tag{3.1}$$

$$y = Y^k \phi_k(\xi), \tag{3.2}$$

where X^k and Y^k denote, in this order, the two (plane) initial and current coordinates of node k, whose associated shape function is ϕ_k; and ξ is the vector that contains the two non-dimensional coordinates (ξ_1 and ξ_2). The plane entries of the deformation gradient $\boldsymbol{F}$ defined in (1) are numerically determined as follows:

$$F = F_1 (F_0)^{-1}, \tag{3.3}$$

$$F_1 = \frac{\partial y}{\partial \xi} = Y^k \frac{\partial \phi_k(\xi)}{\partial \xi}, \tag{3.4}$$

$$F_0 = \frac{\partial x}{\partial \xi} = X^k \frac{\partial \phi_k(\xi)}{\partial \xi}. \tag{3.5}$$

Similar expressions to determine the gradient $\boldsymbol{F}$ can be found, for example, in [31] for the mid-surface of triangular shell elements or in [29] for solid tetrahedral elements. The degrees of freedom of the present finite element are the two current coordinates of the nodes, instead of using the traditional form with nodal displacements.

In order to use the general degree of approximation, the numerical strategy developed on [31] has been adopted. With this strategy, the number and position of the nodes and the shape functions (as well as their derivatives) are automatically determined via simple matrix operations based on the element order employed. The advantage of this procedure becomes more evident especially for high orders, since there is no need to determine analytically all the shape functions and to implement the expressions to calculate them. The automatic shape function generator proposed in [31] can be employed for any triangular finite element.

The plane components of the Cauchy–Green stretch tensor $\boldsymbol{C}$ are numerically determined from expressions (2.2) and (3.3), and the plane components of tensor $\boldsymbol{C}_p$ are assumed to be known for a given instant. As mentioned in Sec. 2, the out-of-plane entry C_{33} is found iteratively from the plane stress condition. After some manipulation and considering (2.27), the last result of expression (2.15) is equivalent to the following expression:

$$f = \frac{C_{11}C_{22} - C_{12}^2}{C_{p11}C_{p22} - C_{p12}^2} = \frac{1}{C_{e33}} \left\{ \exp\left[\frac{\mu}{K}(1 - C_{e33})\right] \right\}^2, \tag{3.6}$$

where f is the auxiliary scalar variable, which can be determined from the plane components of stretch tensors $\boldsymbol{C}$ and $\boldsymbol{C}_p$. However, there is no explicit expression to determine C_{e33} in terms of such components. Applying a simple Newton method, one can determine C_{e33} iteratively using the following expressions:

$$r = \frac{C_{11}C_{22} - C_{12}^2}{C_{p11}C_{p22} - C_{p12}^2} - \frac{1}{C_{e33}} \left\{ \exp\left[\frac{\mu}{K}(1 - C_{e33})\right] \right\}^2, \tag{3.7}$$

$$\frac{dr}{dC_{e33}} = \frac{1}{C_{e33}^2} \left\{ \exp\left[\frac{\mu}{K}(1 - C_{e33})\right] \right\}^2 + \frac{2}{C_{e33}} \frac{\mu}{K} \left\{ \exp\left[\frac{\mu}{K}(1 - C_{e33})\right] \right\}^2, \tag{3.8}$$

$$r + \frac{dr}{dC_{e33}} \Delta C_{e33} = 0 \Rightarrow \Delta C_{e33} = -r \left(\frac{dr}{dC_{e33}} \right)^{-1}. \tag{3.9}$$

Once the component C_{e33} is found, the out-of-plane components can be obtained (see expressions 2.2 and 2.3):

$$C_{33} = F_{33}^2 = F_{p33} C_{e33} F_{p33} = C_{e33} C_{p33} = \frac{C_{e33}}{C_{p11} C_{p22} - C_{p12}^2}. \tag{3.10}$$

3.2. Equilibrium. The equilibrium achieved at the current (deformed) configuration is expressed via the principle of minimum total potential energy (or, equivalently, by the nonlinear version of the principle of virtual work):

$$\delta \Pi = \left(\int_{\Omega_0} \frac{\partial \psi}{\partial Y} dV_0 - f_{\text{ext}} \right) \delta Y = 0 \Rightarrow f_{\text{int}} = \int_{\Omega_0} \frac{\partial \psi}{\partial Y} dV_0 = f_{\text{ext}}, \tag{3.11}$$

where δ represents the virtual variation; dV_0 is the volume element at the initial domain Ω_0; Y denotes the vector that contains the degrees of freedom; and f_{ext} is the vector of external (applied) forces, which are assumed to conservative in the present study. The system defined in the result of (3.11) is nonlinear regarding the current nodal positions and, thus, the Newton-Raphson iterative technique is employed:

$$r = f_{\text{int}} - f_{\text{ext}} = \int_{\Omega_0} \frac{\partial \psi}{\partial Y} dV_0 - f_{\text{ext}}, \tag{3.12}$$

$$H = \frac{\partial r}{\partial Y} = \int_{\Omega_0} \frac{\partial^2 \psi}{\partial Y \partial Y} dV_0, \tag{3.13}$$

$$\Delta Y = -H^{-1} \cdot r, \tag{3.14}$$

where r is the residual force vector; and H is the Hessian matrix. The positional vector Y is updated via (3.14) until the residual vector r is sufficiently small. Alternative expressions for the internal force vector and for the Hessian matrix can be written:

$$f_{\text{int}} = \int_{\Omega_0} \frac{\partial \psi}{\partial C} : \frac{\partial C}{\partial Y} dV_0 = \frac{1}{2} \int_{\Omega_0} S : \frac{\partial C}{\partial Y} dV_0, \tag{3.15}$$

$$H = \frac{1}{2} \int_{\Omega_0} \left(\frac{\partial S}{\partial C} : \frac{\partial C}{\partial Y} : \frac{\partial C}{\partial Y} + S : \frac{\partial^2 C}{\partial Y \partial Y} \right) dV_0. \tag{3.16}$$

One can note, in the above expressions, the separation between the kinematic approximation and the constitutive law. The derivatives of stretch tensor C in respect to Y are determined from the finite element approach. The stress tensor S and the consistent tangent operator $\partial S / \partial C$ are calculated based on the material model.

Since all the stress and strain measures do not vary along the thickness direction, the volume integrals that appear in (3.15) and (3.16) can be replaced by surface integrals. Besides, considering the positional approximation described in Sec. 3.1, the volume integrals are calculated as follows:

$$\int_{\Omega_0} g dV_0 = b_0 \int_{A_0} g dA_0 = b_0 \int_{\xi} g J_0 d\xi_1 d\xi_2, \tag{3.17}$$

where g is the general function to be integrated over the initial volume domain; b_0 is the initial thickness of the element (assumed to be the same for all elements); dA_0 is the surface element; and J_0 is the initial Jacobian, defined as $J_0 = \det F_0$. The surface integrals defined in (3.17) are numerically evaluated by using Gaussian quadrature rules.

3.3. Elastic Predictor. The elastoplastic problem is solved by the usual method, in which a dual-step procedure is employed: an elastic prediction phase followed by a plastic correction. In the first phase, the deformation is assumed to be purely elastic, i.e., no plastic strain occurs. Therefore, the consistent tangent operator in (3.16) is determined considering only possible variations of the stretch tensor C and all the derivatives regarding the plastic tensor C_p are neglected. From (2.17), one can obtain the elastic consistent tangent operator for the present model:

$$\frac{\partial S}{\partial C} = \mu \left(-C^{-1} \otimes \frac{\partial C_{e33}}{\partial C} - C_{e33} \frac{\partial C^{-1}}{\partial C} \right), \tag{3.18}$$

where $\otimes$ denotes the tensor product. The derivative $\partial C^{-1} / \partial C$ can be obtained from the inverse matrix of (2.3):

$$C^{-1} = \frac{1}{C_{11}C_{22} - C_{12}^2} \begin{bmatrix} C_{22} & -C_{12} \\ -C_{12} & C_{11} \end{bmatrix}. \tag{3.19}$$

Some care should be taken with the derivative $(\partial C_{e33}) / (\partial C)$, since the entry C_{e33} depends implicitly on the plane stretch components. To solve this problem, derivative $(\partial C_{e33}) / (\partial C)$ is obtained from (3.6):

$$\frac{\partial C_{e33}}{\partial C} = \frac{\partial C_{e33}}{\partial f} \frac{\partial f}{\partial C} = \left(\frac{\partial f}{\partial C_{e33}} \right)^{-1} \frac{\partial f}{\partial C}, \tag{3.20}$$

$$\frac{\partial f}{\partial C_{e33}} = -2\frac{\mu}{k} \frac{\left\{ \exp\left[\frac{\mu}{k}(1-C_{e33}) \right] \right\}^2}{C_{e33}} - \frac{\left\{ \exp\left[\frac{\mu}{k}(1-C_{e33}) \right] \right\}^2}{C_{e33}^2}, \tag{3.21}$$

$$\frac{\partial f}{\partial C} = \frac{1}{\left(C_{p11}C_{p22} - C_{p12}^2 \right)} \begin{bmatrix} C_{22} & -C_{12} \\ -C_{12} & C_{11} \end{bmatrix}. \tag{3.22}$$

3.4. Plastic Correction. After calculating the stress tensor S, the yield criterion (2.19) is verified at all integration points. If condition (2.19) is not satisfied, a plastic correction is performed to update the plastic stretch tensor C_p, the isotropic hardening parameter κ and the initial backstress tensor X. To this end, the radial return algorithm based on the implicit backward Euler method is employed. From the evolution equations (2.25) and (2.29), the following expressions are used together with (2.19):

$$C_p^{N+1} = C_p^N + \Delta\gamma R_{cp}^{N+1}, \tag{3.23}$$

$$X^{N+1} = X^N + \Delta\gamma R_X^{N+1}, \tag{3.24}$$

where $N+1$ and N denote the end and the beginning of step N, respectively. As in the case of equilibrium system (3.11), the Newton–Raphson iterative procedure is employed in the plastic correction phase. The plastic variables $\{C_{p11}, C_{p12}, C_{p22}, \Delta\gamma, X_{11}, X_{12}, X_{22}, X_{33}\}$ are updated until expressions (2.19), (3.23) and (3.24) are satisfied. Because of (2.22) and (2.23), the isotropic hardening parameter has a linear relation with the plastic multiplier increment:

$$\kappa^{N+1} = \kappa^N + \Delta\gamma\sqrt{2/3}. \tag{3.25}$$

Thus, whenever the above plastic set is updated, the plastic stretch C_{p33} and parameter κ are automatically determined from (2.27) and (3.25), respectively.

3.5. Hyperelastoplastic Consistent Tangent Operator. For the numerical integration points at which the plastic correction has been performed, the derivative of stresses regarding the plastic stretch tensor C_p is included:

TABLE. Isoparametric triangular membrane elements employed

Element order	Number of nodes per element	Number of integration points per element
1	3	1
2	6	13
3	10	16
4	15	19

$$\frac{\partial \boldsymbol{S}}{\partial \boldsymbol{C}} = \left(\frac{\partial \boldsymbol{S}}{\partial \boldsymbol{C}}\right)^{EL} + \frac{\partial \boldsymbol{S}}{\partial \boldsymbol{C}_p} : \frac{\partial \boldsymbol{C}_p}{\partial \boldsymbol{C}}, \tag{3.26}$$

$$\frac{\partial \boldsymbol{S}}{\partial \boldsymbol{C}_p} = \mu \left(\frac{\partial \boldsymbol{C}_p^{-1}}{\partial \boldsymbol{C}_p} - \boldsymbol{C}^{-1} \frac{\partial \boldsymbol{C}_{e33}}{\partial \boldsymbol{C}_p}\right), \tag{3.27}$$

$$\frac{\partial \boldsymbol{C}_p}{\partial \boldsymbol{C}} = \boldsymbol{R}_{cp} \otimes \boldsymbol{B}, \tag{3.28}$$

where the superscript *EL* denotes the elastic consistent tangent operator (3.18); and matrix $\boldsymbol{B}$ is the second-order tensor derived from the consistency condition:

$$\dot{\phi} = \frac{\partial \phi}{\partial \boldsymbol{C}} : \dot{C} + \frac{\partial \phi}{\partial \boldsymbol{C}_p} \dot{C}_p + \frac{\partial \phi}{\partial \kappa} : \dot{\kappa} + \frac{\partial \phi}{\partial \boldsymbol{X}} : \dot{X} = 0 \Rightarrow \dot{\gamma} = B : \dot{C} \Rightarrow C_p = (B : \dot{C}) \boldsymbol{R}_{cp} = (\boldsymbol{R}_{cp} \otimes \boldsymbol{B}) : \boldsymbol{C}, \tag{3.29}$$

$$\boldsymbol{B} = -\frac{\dfrac{\partial \phi}{\partial \boldsymbol{C}}}{\dfrac{\partial \phi}{\partial \boldsymbol{C}_p} : \boldsymbol{R}_{cp} + \dfrac{\partial \phi}{\partial \kappa} : \sigma_\kappa + \dfrac{\partial \phi}{\partial \boldsymbol{X}} : \boldsymbol{R}_X}. \tag{3.30}$$

The derivative $(\partial \boldsymbol{C}_p^{-1})/(\partial \boldsymbol{C}_p)$ and $(\partial \boldsymbol{C}_{e33})/(\partial \boldsymbol{C}_p)$ can be found as in (3.19) and (3.20):

$$\boldsymbol{C}_p^{-1} = \frac{1}{C_{p11}C_{p22} - C_{p12}^2} \begin{bmatrix} C_{p22} & -C_{p12} \\ -C_{p12} & C_{p11} \end{bmatrix}, \tag{3.31}$$

$$\frac{\partial \boldsymbol{C}_{e33}}{\partial \boldsymbol{C}_p} = \frac{\partial \boldsymbol{C}_{e33}}{\partial f} \frac{\partial f}{\partial \boldsymbol{C}_p} = \left(\frac{\partial f}{\partial \boldsymbol{C}_{e33}}\right)^{-1} \frac{\partial f}{\partial \boldsymbol{C}_p}, \tag{3.32}$$

$$\frac{\partial f}{\partial \boldsymbol{C}_p} = -\frac{(C_{11}C_{22} - C_{12}^2)}{(C_{p11}C_{p22} - C_{p12}^2)^2} \begin{bmatrix} C_{p22} & -C_{p12} \\ -C_{p12} & C_{p11} \end{bmatrix}. \tag{3.33}$$

Because of the plane stress condition, the fourth order tensors have dimensions $2 \times 2 \times 2 \times 2$. The derivatives of the yield function ϕ in terms of $C, \boldsymbol{C}_p, \kappa,$ and $\boldsymbol{X}$ are provided in Appendix A.

Fig. 1. Cook's membrane: geometry, boundary conditions and material coefficients. Dashed lines denote base mesh. Point B has coordinates $x_1 = 4$ and $x_2 = 41.3333$ (regarding the left bottom corner).
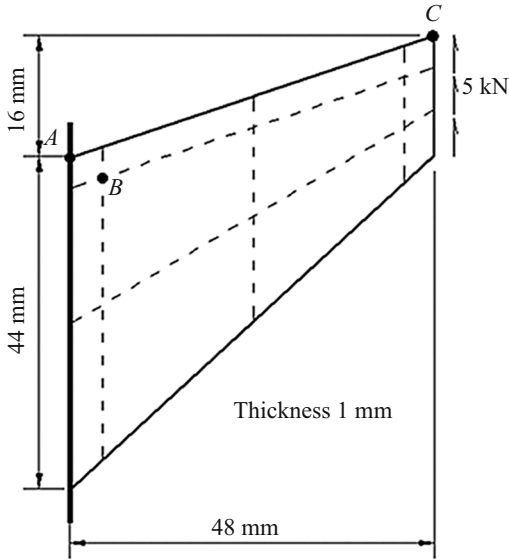
Model	Neo-Hookean (2.10)		Voce (2.21)			
Coefficient	K	μ	Y_0	Y_{sat}	β	H
Value	164.21	80.1938	0.45	0.715	16.93	0.12924
Unit	GPa	GPa	GPa	GPa	—	GPa

4. Results and Discussion. Four structural problems involving finite elastoplastic strains and plane stress conditions are numerically analyzed in order to test the performance of the present approach. The numerical formulation described in this paper has been implemented in a computer code and the simulations have been performed in a cluster with 12 processors.

A series of discretizations is employed for each problem, varying the quantity and the order of the elements. Thus, both hierarchical and polynomial enrichments are used in order to show the influence of the mesh refinement on the structural behavior. The different meshes of each example are automatically generated from the same base mesh composed of linear order quadrilaterals, which are transformed into triangular finite elements based on the number of edge divisions and the polynomial degree adopted. In this study, four approximation orders have been employed together with full integration (see Table).

The prescribed load (or displacement) is divided into a large number of steps in order to improve convergence and stability. An error tolerance of 10^{-6} has been employed for the following quantities: the norm of the residual force vector (3.12); the yield function (2.19); and the norm of the residual vector from the plastic correction phase (see Sec. 3.4).

Along the main simulation, the nodal positions (Y_1 and Y_2) and the plastic parameters ($C_{p11}, C_{p12}, C_{p22}$, κ, X_{11}, X_{12}, X_{22}, and X_{33}) are stored at the numerical integration points at the end of some steps. In a post-processing program, the values at these points are transferred to the nodes via a linear extrapolation based on the least squares method. The resultant nodal values are used to plot the distributions of stress and strain components by means of the AcadView software [27].

4.1. Cook's Membrane. The first example is the Cook's membrane showed in Fig. 1. This benchmark problem has been extensively used to test finite element approaches in bending-dominated problems. The stress concentration near the left upper corner (point A) increases considerably the complexity of the analysis. The objective here is to assess the numerical formulation in a plane stress problem involving large elastoplastic strains, bending, shearing and a singularity point. Many plane strain formulations have been employed to solve this example in large elastoplastic deformation, such as the assumed enhanced formulation of [13] and the B/bar elements of [5]. Plane stress conditions are assumed, for example, in [37], in which a geometrically linear elastoplastic analysis is performed based on the assumed enhanced method. To analyze the present problem, only isotropic hardening based on a saturation law is considered. The applied force is uniformly distributed along the edge $x_1 = 48$ mm and is always vertical (not tangential to the deformed edge). The material coefficients and the value of the prescribed force are extracted from [13] and [5]. The base mesh depicted in Fig. 1 has been proposed to enrich the kinematics near the singularity point.

The convergence analysis is performed considering the final displacements of the right top corner C, as well the final isotropic hardening parameter κ at points A and B. As expected, the displacements converge with mesh refinement and the convergence rate is improved by increasing the element order, see Fig. 2a and 2b. The final vertical displacement converges to 10.55 with the present plane stress formulation and to approximately 7.0 in the plane strain references [13] and [5]. This difference is probably due to the plane assumption adopted in each work. Regarding the final displacements of the right top
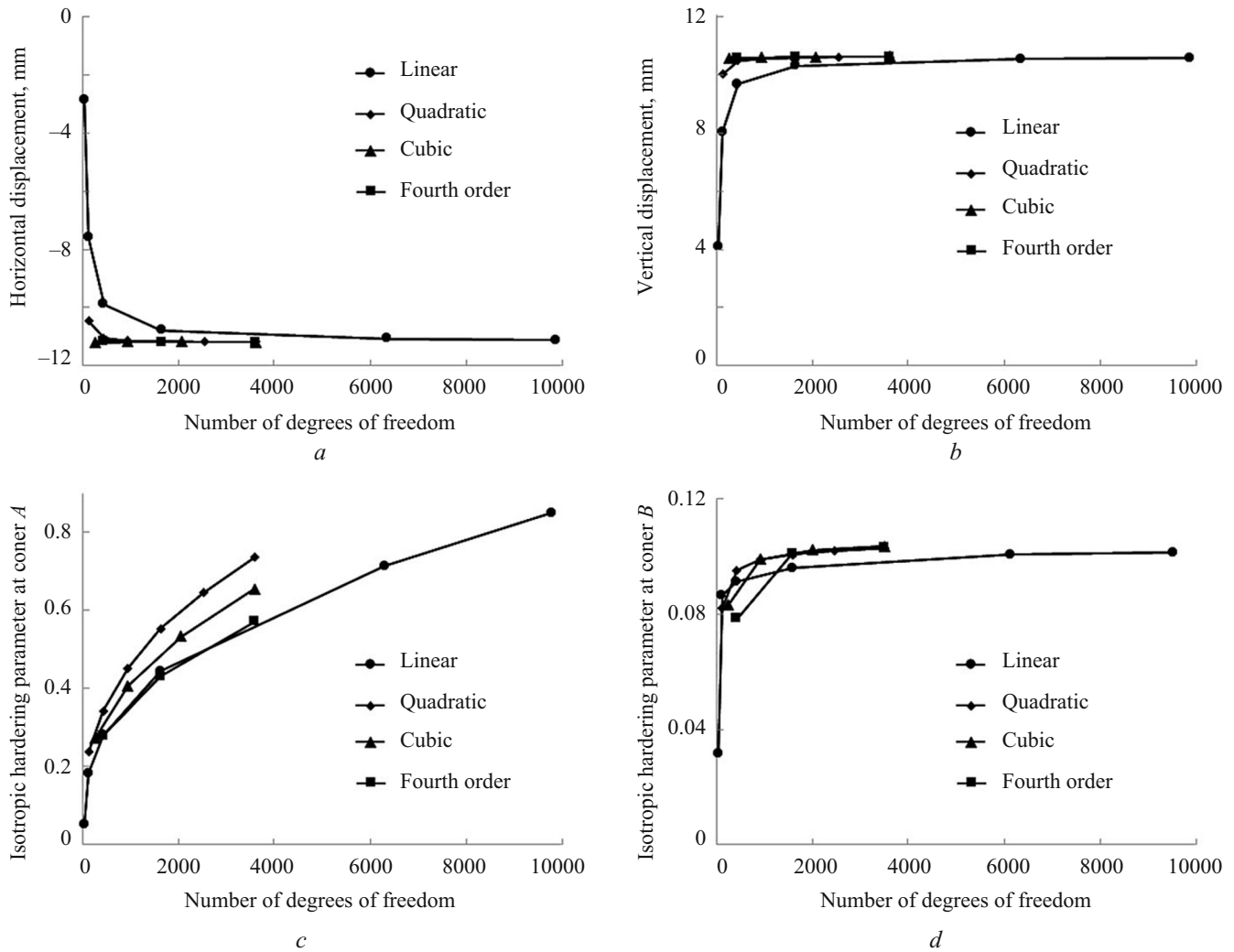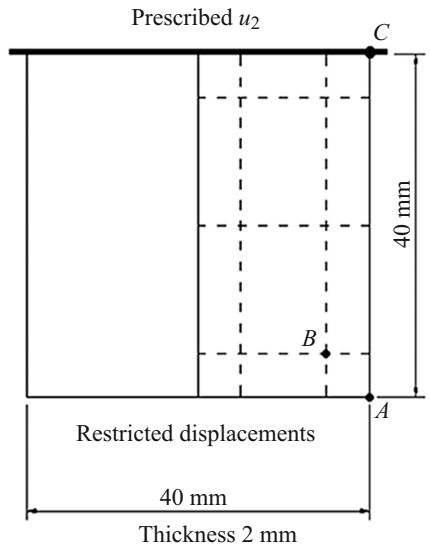
Fig. 2. Convergence analysis regarding final values for the Cook's membrane.

corner, the best convergence rates obtained in such references are similar to the present quadratic order depicted in Fig. 2. In other words, the performance of linear order elements can be improved by increasing the polynomial degree or by using mixed-enhanced strain formulations. However, the present cubic and fourth order elements provide a higher convergence rate when compared to those references, since the displacements are practically the same even for meshes with few elements. Results of Fig. 2a and 2b also indicate that the convergence is always monotonous for all the orders, except for the final horizontal displacement provided by the less refined cubic mesh.

In terms of the final isotropic hardening parameter, the convergence is more difficult at the singularity A when compared to point B (see Fig. 2c and 2d) due to the expected complex strain and stress fields around the left upper corner. One can also observe that the graphs indicate that the convergence will be achieved by increasing even more the number of degrees of freedom for each element order. In addition, the convergence analysis regarding the isotropic hardening parameter is rarely done in scientific literature.

4.2. Block Upsetting. The second example is the square block under compression depicted in Fig. 3. This problem has been studied under the assumption of plane strain conditions, for example, in [5] and [9], in which quadrilateral elements based on the enhanced strain method are used. The difficulty in analyzing this problem is the possible occurrence of hourglass instabilities, because of the moderately large levels of compression. The material is assumed to be purely elastic in [9] and elastic-perfectly plastic in [5]. In the present work, the material response of the block includes hyperelastic behavior together with mixed hardening. The material coefficients have been extracted from [23] considering the mild steel CK15. The same material data have been employed in [43] to show numerically the Bauschinger effect in cyclic loading.

Model	Neo-Hookean (2.10)		Armstrong–Frederick (2.24)		Voce (2.21)		
Coefficient	K	μ	c	b	Y_0	Y_{sat}	β
Value	119.999	80	1.9	8.5	300	700	2.5
Unit	GPa	GPa	GPa	—	MPa	MPa	—

Fig. 3. Block upsetting: geometry, boundary conditions and material data.
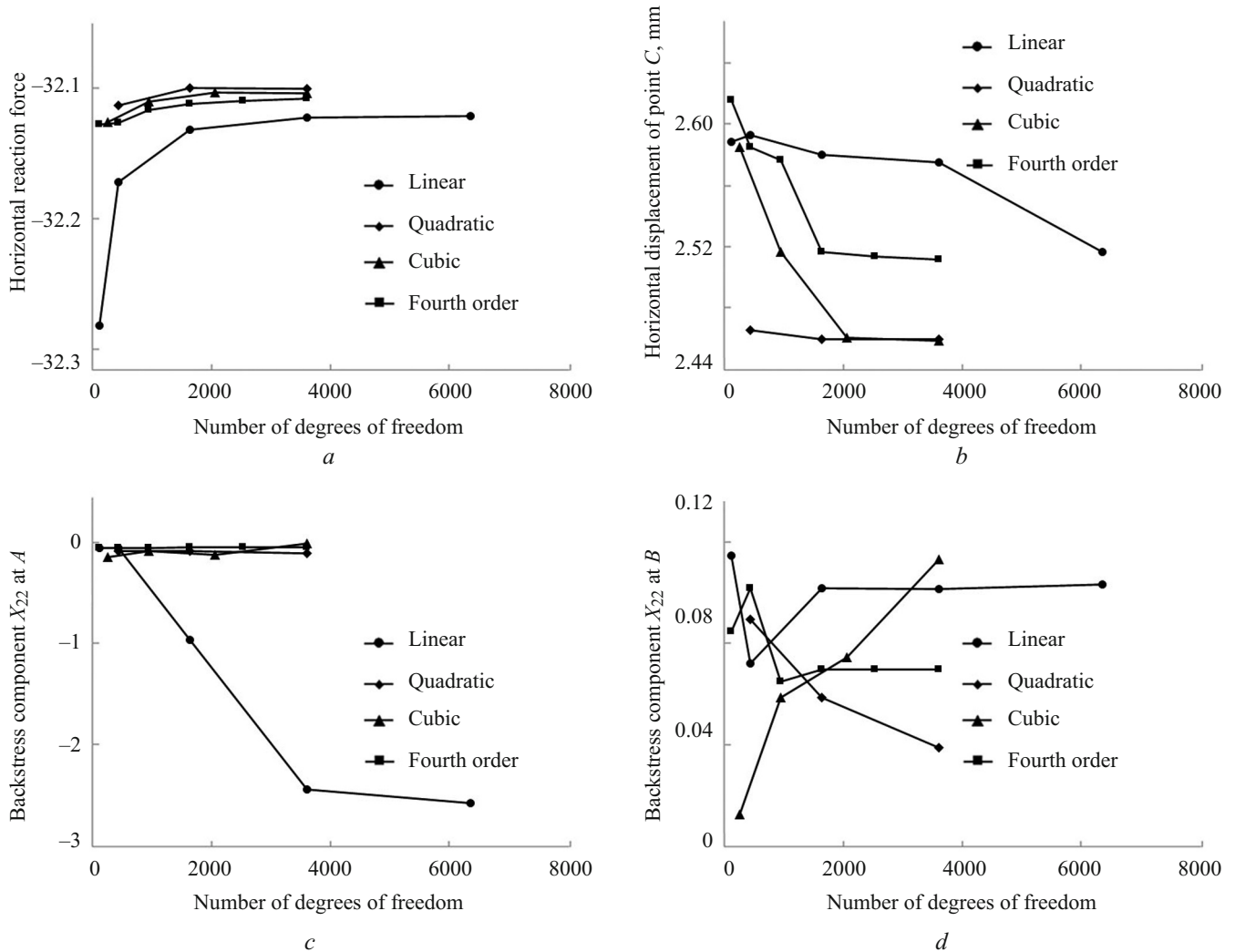
Fig. 4. Convergence analysis regarding final values for block upsetting.

Fig. 5. Necking of tensile specimen: geometry, boundary conditions and material data.
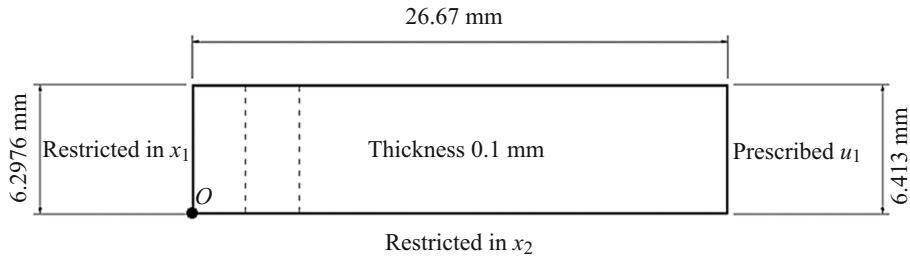
Model	Neo-Hookean (2.10)		Swift (2.20)		
Coefficient	K	μ	Y_s	ε_0	n
Value	68.6275	26.3158	0.42363	0.00380602	0.0549
Unit	GPa	GPa	GPa	—	—

The level of upsetting displacement, in terms of the initial height, reaches 16% in the present paper, 30% in [9] and 10% in [5]. Such compression levels can be considered moderately high for metals and, since the deformation is not homogeneous, mesh distortions take place. Thus, the possible occurrence of hourglass instabilities should be investigated. Due to the symmetry regarding the center vertical line, only one half of the problem is discretized and the horizontal displacements of the symmetry plane are restricted. The bottom face is constrained along the two directions and the horizontal displacements of the upper face are released. All the simulations of this problem have been performed via a uniform vertical displacement control. The total vertical reaction force is computed at the end of each step considering the vertical forces of all the nodes at the upper face.

For the present example, the convergence analysis is performed in terms of the final vertical reaction force, the horizontal displacement of point C and the vertical backstress component X_{22}. According to Fig. 4a, the reaction forces become smaller when the mesh is refined. Thus, as in the Cook's membrane problem, mesh refinement yields more flexibility. Even the coarse discretizations provide a quite accurate result in terms of the final reaction force. The linear order meshes seem to converge to a stiffer solution, presenting a questionable performance in the present example. One should highlight that no convergence analysis is performed in [5] and [9], in which a 10×10 and 23×23 element regular meshes are employed, respectively. Only comparisons among quadrilateral finite element formulations are made in such works.

According to Fig. 4b, the final horizontal displacement of point C provided by the linear and quadratic meshes presents slower convergence rate, comparing to the cubic and fourth-order elements. The converged value is approximately 2.46 mm (to the right), which indicates the barreling of the sample, since the right bottom corner A does not move.

The convergence analysis performed in terms of the vertical backstress component depicted in Fig. 4c and 4d shows that further investigations should be done. While the convergence rate is quite acceptable at point A (except for the linear order), the converged values at point B are clearly different for each element order. Such difficulty is probably related to the highly nonlinear character of the large-strain model adopted.

4.3. Necking. Next, the necking of a specimen under plane stress conditions is analyzed (see Fig. 5). This example has been widely studied to investigate the plastic necking zones.

The geometry and the boundary conditions are the same as those adopted in [13, 19, 37] and [5]. Following the usual procedure, a linearly variable width reduction is employed to trigger the necking and the mesh refinement is higher on the region with expected stress concentration. The material data have been extracted from tensile test data of aluminum alloy 6351, considering only isotropic hardening.

Discretizations with 192 and 432 finite elements are employed to analyze the present problem. According to Fig. 6, the flexibility is increased by mesh refinement. The linear order meshes have lost convergence after reaching the peak load at a
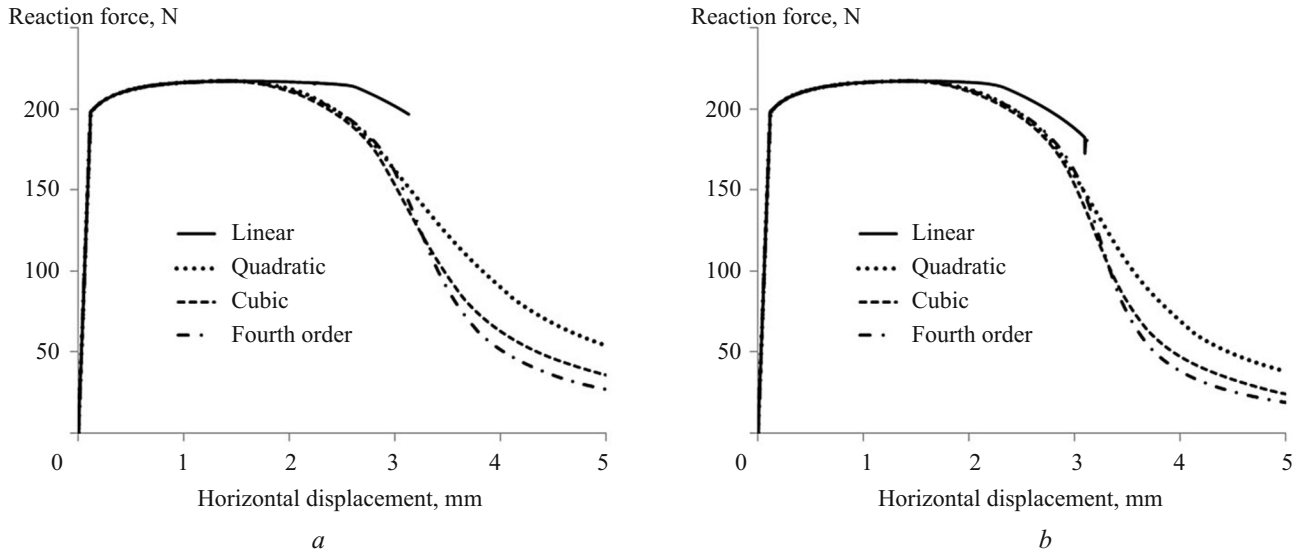
114

Fig. 6. Convergence analysis regarding reaction forces for the necking problem: 192 elements (*a*) and 432 elements (*b*).
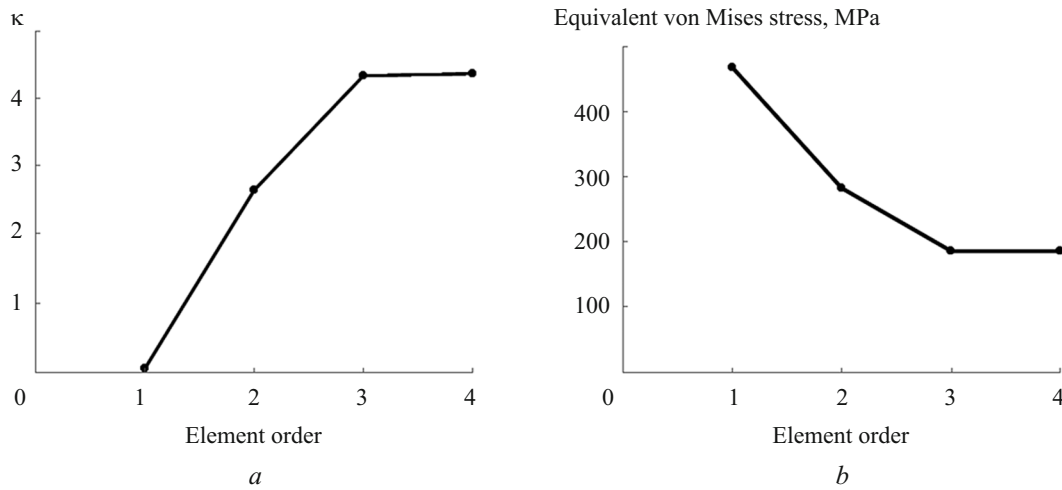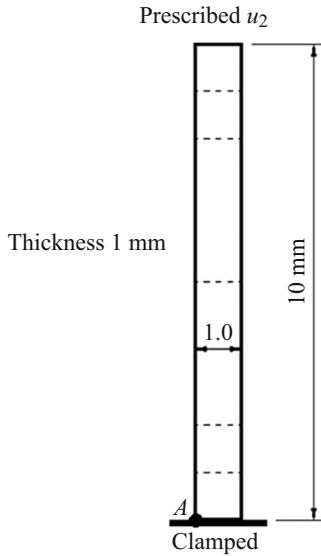

Fig. 7. Convergence analysis regarding final values at origin *O* for necking problem discretized with 432 elements.

displacement level of approximately 3.12 mm. The maximum load achieved considering the most refined mesh (3577 nodes and 432 fourth order elements) is 217.2 N at a displacement level of 1.44 mm. These values correspond to a nominal longitudinal stress of 338.7 MPa and an engineering longitudinal strain of 5.4%. The applied load is approximately constant between displacement levels of 1.2 and 1.5 mm for all the meshes (except for the linear order elements) indicating that, along this stage, the increase in the yield stress limit compensates the cross-sectional area reduction of the necking zone. One can also observe that, except for the linear order, the curves become clearly different along the necking stage.

The present load-displacement curves are different from the plane stress references [37] and [19], in which the reaction forces fall more quickly after the peak load is reached. The material coefficients adopted in such references are the same as those in the present work, although the model is different in terms of the strain and stress measures adopted. The peak level of the load displacement curve is achieved at $u_1 = 2.8$ mm and $u_1 = 3.1$ mm in [37] and [19], respectively.

For the meshes with 432 elements, the influence of the element order on the final values of the following quantities at the origin *O* is studied: the isotropic hardening parameter κ; and the equivalent von Mises stress:

$$\sigma_{eq} = \sqrt{\frac{3}{2} \mathbf{dev\sigma} . \mathbf{dev\sigma}}. \tag{4.1}$$

115

Fig. 8. Buckling of clamped column: geometry, boundary conditions and material data.

Model	Neo-Hookean (2.10)		Armstrong– Frederick (2.24)		Initial yield stress
Coefficient	K	μ	c	b	σ_k
Value	320	80	100	2.7	35
Unit	MPa	MPa	MPa	—	MPa

The reason of adopting that point is the expected initial occurrence of the shear banding, which leads to a complex state and possible instabilities. Figure 7 shows that both hardening parameter and equivalent stress converge by increasing the element order, considering the meshes with 432 elements.

4.4. Buckling. The last example is the buckling of the clamped column shown in Fig. 8. The objective is to investigate if the present finite element technique is capable of reproducing the post-buckling behavior. The base mesh shown in Fig. 8 has been proposed to enrich the kinematics near the ends and to avoid very elongated elements. To trigger the buckling instability, an eccentricity linearly variable along the length is adopted, reaching the value of 0.1% at the top face. Alternative strategies can be employed to trigger the buckling. In [20], for example, a clamped-clamped beam composed of a hyperelastic material is analyzed in plane strain conditions and the buckling instability is reproduced by using a small horizontal force. In the present work, the clamped condition of the bottom face is imposed by restricting the plane displacements of the nodes. The material data have been extracted from [10] considering the kinematic hardening of a glassy polymer called oriented PET. All the simulations have been performed via a vertical displacement control uniformly applied to the top face.

The convergence analysis is done with respect to the final horizontal displacement of the top face and the vertical reaction force, as well as the equivalent stress (4.1) and backstress component X_{22} at point A. As expected, the coarse discretizations of linear degree present severe locking and the convergence rate is improved by increasing the order, expect for one cubic and one fourth order mesh, see Fig. 9a and 9b. However, the converged solutions are approximately the same for all the orders employed. In [20], the alternative technique called domain-boundary element method (DBEM) is used to analyze a buckling problem. Their results, based on four and eight-node quadrilateral elements, are in good agreement with the FEM regarding displacements and stresses. The required number of degrees of freedom in the buckling problem of that work is approximately 500, which is similar to the present results, except for the linear order. Moreover, the high levels of final free-end horizontal displacement indicate that the column becomes unstable (or buckles).

In terms of the final equivalent stress at point A, a slight oscillation occurs for coarse meshes, although it seems that convergence is achieved for sufficiently refined discretizations (Fig. 9c). For the present example, the final value of the vertical backstress component X_{22} at point A clearly converges with mesh refinement. These aspects show that the present formulation is capable of providing a good accuracy regarding such stress and backstress measures, even in problems involving unstable behavior.

Conclusions. A finite element formulation for the analysis of elastoplastic materials under finite strain levels and plane stress conditions is developed in the present work. The constitutive model is defined within a Lagrangian isotropic hyperelastoplastic framework based on the multiplicative split of the deformation gradient, accounting for finite elastoplastic strains and nonlinear mixed hardening rules. The condensation of the 3D model into a compact 2D form, based on the plane stress condition $\sigma_{33} = 0$, yields an implicit relationship between the stresses and the right Cauchy–Green stretch components,
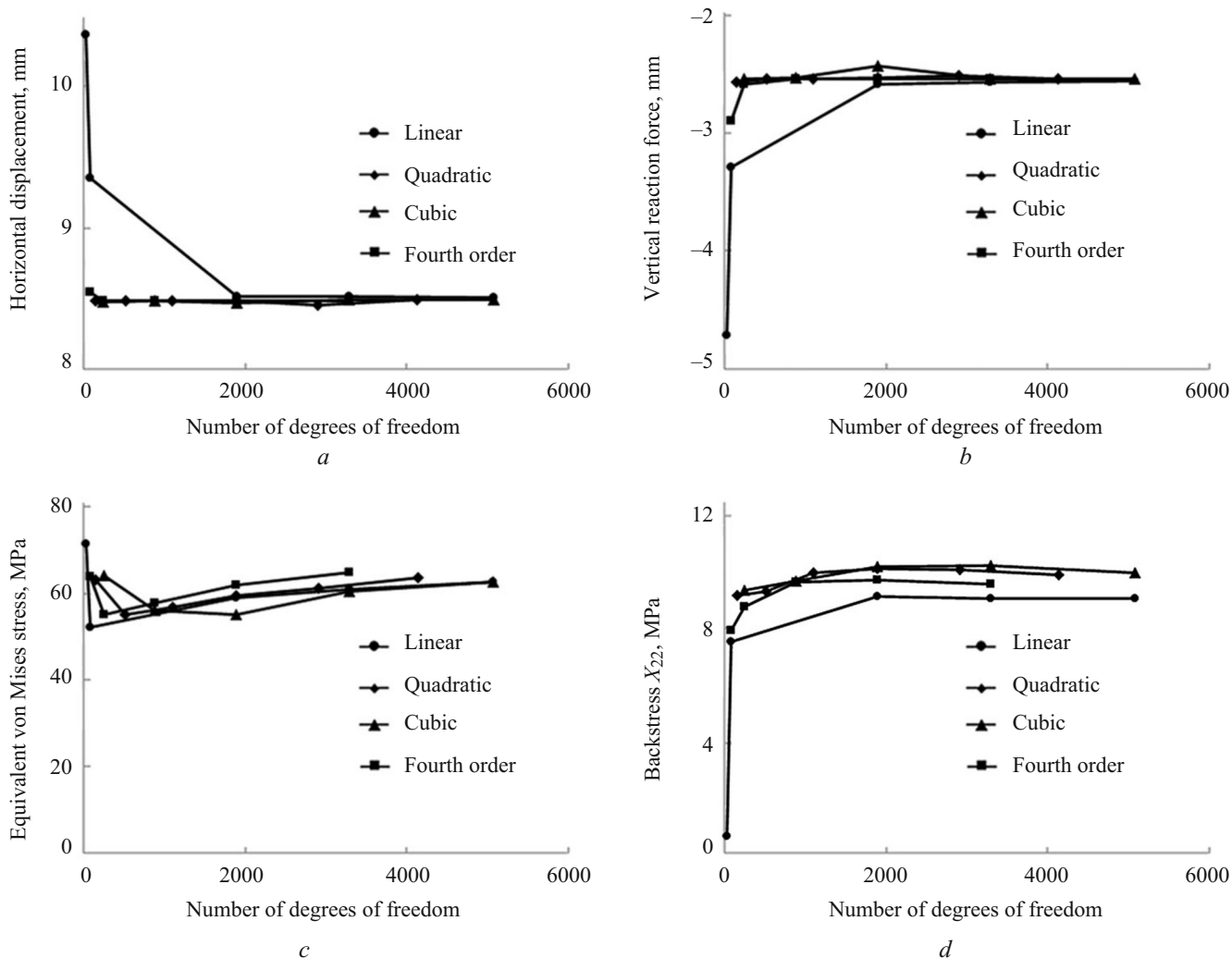
Fig. 9. Convergence analysis for buckling problems regarding final values at top face.

which is solved numerically. The hyperelastoplastic consistent tangent operator is defined as a fourth-order tensor with dimensions $2 \times 2 \times 2 \times 2$, avoiding the determination of the complete 3D tensor (with dimensions $3 \times 3 \times 3 \times 3$). Since the transverse stretch C_{33} cannot be explicitly determined from the plane stretch entries, an auxiliary scalar variable involving all the components had to be incorporated into the calculation of the tangent operator. As pointed out, although the condensation is relatively simple, some care should be taken in order to determine the tangent operator, since the derivatives of the out-of-plane stretch component regarding the plane entries need to be implicitly included. The specific 2D constitutive expressions developed in this work can be employed, for example, in a user-defined material subroutine to model hyperelastoplastic materials under plane stresses. Besides, the implementation of other elastoplastic models (including yield function, damage coupling, non-associative flow rules, hardening behavior or even anisotropy) may be easily performed following the procedure presented in the present paper, which consists of condensation of the material law and a proper method to compute the derivatives needed in the numerical solution of the resultant nonlinear problem.

The plane kinematical approximation is based on the isoparametric triangular membrane element of any-order based on positional description. Although the formulation is standard, it allows refinement in terms of the polynomial degree in a general way (using the same computer code). Four structural examples involving plane stress and large elastoplastic deformation have been analyzed to validate the present approach: the Cook's membrane, a block upsetting, the necking problem and a column under buckling. Results indicate that, as expected, mesh refinement improves accuracy. The element order increases up to fourth order and it is shown that, in general, the linear approximation provides severe locking behavior and poor convergence rate in terms of displacements, forces and stresses, as well as isotropic hardening parameter and backstress components. Increasing the

117

polynomial order and using the full integration scheme have shown to be an effective way of avoiding unrealistic stiffness (locking) and spurious zero-energy modes (hourglass instabilities) even in non-trivial problems involving singularity point, stress concentration, bending, mesh distortions and post-buckling. Along the simulations, the required number of degrees of freedom can be considered relatively small, indicating that a reliable solution can be achieved with a reasonable computational effort. Therefore, the present formulation is robust, simple and accurate. Moreover, the numerical results presented can serve as a basis (or a parameter of choice) for engineers who need to select a proper element order to simulate plane stress problems involving elastoplastic materials.

The main contribution of the present paper is the investigation of the mechanical behavior of various element orders in the context of large elastoplastic strains, mixed hardening and plane stress conditions. As far as the author knows, this is the first work in which the element performance of low and high orders is assessed, considering the present context. Future studies regarding the implementation of other large-strain constitutive models in plane stress conditions (e.g. anisotropic, non-associative elastoplastic, damage-coupled, viscoelastic, thermoelastic, incompressible materials etc.) are the next objectives of the present author.

Appendix A – Derivatives of Yield Function. The derivatives of the yield function (19) regarding the stretch tensor C and the plastic parameters C_p, κ, and, X are provided in this section. First, the derivative of ϕ in terms of the auxiliary tensor $Y = CS - C_p X$ is obtained:

$$\frac{\partial \phi}{\partial Y} = \frac{\partial}{\partial Y} ||\text{dev} Y|| = \frac{\text{dev} Y}{||\text{dev} Y||} : \frac{\partial \text{dev} Y}{\partial Y} = \frac{\text{dev} Y}{||\text{dev} Y||} : \left(II - \frac{1}{3} I \otimes I \right). \tag{A1}$$

Next, the derivatives of Y are determined in index notation:

$$\frac{\partial Y_{ij}}{\partial C_{kl}} = \frac{\partial}{\partial C_{kl}} (C_{im} S_{mj}) = \delta_{ik} S_{lj} + C_{im} \frac{\partial S_{mj}}{\partial C_{kl}}, \tag{A2}$$

$$\frac{\partial Y_{ij}}{\partial (C_p)_{kl}} = -\frac{\partial}{\partial (C_p)_{kl}} \left[(C_p)_{im} X_{mj} \right] = -\delta_{ik} X_{lj}, \tag{A3}$$

$$\frac{\partial Y_{ij}}{\partial X_{kl}} = -\frac{\partial}{\partial X_{kl}} \left[(C_p)_{im} X_{mj} \right] = -(C_p)_{ik} \delta_{jl}. \tag{A4}$$

Combining expressions (A1)–(A4) yields the following derivatives:

$$\frac{\partial \phi}{\partial C} = \frac{\partial \phi}{\partial Y} : \frac{\partial Y}{\partial C}, \tag{A5}$$

$$\frac{\partial \phi}{\partial C_p} = \frac{\partial \phi}{\partial Y} : \frac{\partial Y}{\partial C_p}, \tag{A6}$$

$$\frac{\partial \phi}{\partial X} = \frac{\partial \phi}{\partial Y} : \frac{\partial Y}{\partial X}. \tag{A7}$$

The remaining derivative is easily obtained from (19):

$$\frac{\partial \phi}{\partial \kappa} = -\sqrt{\frac{2}{3}} \frac{\partial \sigma_\kappa}{\partial \kappa}, \tag{A8}$$

$$\frac{\partial \sigma_\kappa}{\partial \kappa} = Kn(\varepsilon_0 + \kappa)^{n-1} \quad \text{for Swift model (20),} \tag{A9}$$

$$\frac{\partial \sigma_\kappa}{\partial \kappa} = \beta (Y_{sat} - Y_0) \exp^{-\beta\kappa} + H \quad \text{for Voce model (21)}. \tag{A10}$$

As in the case of the derivative $\partial C_{e33} / \partial C$, some care should be taken for the derivative of the entry Y_{33} in terms of C_p (see expression 27):

$$\frac{\partial Y_{33}}{\partial C_p} = -\frac{\partial}{\partial C_p}(C_{p33} X_{33}) = -X_{33}\frac{\partial C_{p33}}{\partial C_p}, \tag{A11}$$

$$\frac{\partial C_{p33}}{\partial C_p} = -\frac{1}{\left(C_{p11}C_{p22} - C_{p12}^2\right)^2}\begin{bmatrix} C_{p22} & -C_{p12} \\ -C_{p12} & C_{p11} \end{bmatrix} = -\frac{1}{\left(C_{p11}C_{p22} - C_{p12}^2\right)^2}\operatorname{adj} C_p, \tag{A12}$$

where adj( ) denotes the adjugate matrix.

REFERENCES

1. L. Anand, "A large deformation poroplasticity theory for microporous polymeric materials," *J. Mech. Phys. Solids*, **98**, 126–155 (2017).
2. P. Areias, D. Dias-da-Costa, J. M. Sargado, and T. Rabczuk, "Element-wise algorithm for modeling ductile fracture with the Rousselier yield function," *Comput. Mech.*, **52**, No. 6, 1429–1443 (2013).
3. P. Areias, M. A. Msekh, and T. Rabczuk, "Damage and fracture algorithm using the screened Poisson equation and local remeshing," *Eng. Fract. Mech.*, **158**, 116–143 (2016).
4. P. Areias, T. Rabczuk, and P. P. Camanho, "Finite strain fracture of 2D problems with injected anisotropic softening elements," *Theor. Appl. Fract. Mech.*, **72**, 50–63 (2014).
5. J. M. A. César de Sá, P. M. A. Areias, and R. M. Natal Jorge, "Quadrilateral elements for the solution of elasto-plastic finite strain problems," *Int. J. Numer. Meth. Eng.*, **51**, 883–917 (2001).
6. H. B. Coda and M. A. Greco, "A simple FEM formulation for large deflection 2D frame analysis based on position description," *Comput. Meth. Appl. Mech. Eng.*, **193**, 3541–3557 (2004).
7. H. B. Coda and R. R. Paccola, "An alternative positional FEM formulation for geometrically non-linear analysis of shells: curved triangular isoparametric elements," *Comput. Mech.*, **40**, No. 1, 185–200 (2007).
8. B. D. Coleman and W. Noll, *The Thermodynamics of Elastic Materials with Heat Conduction and Viscosity. The Foundations of Mechanics and Thermodynamics*, 145–156, Springer Berlin Heidelberg (1974).
9. M. A. Crisfield., G. F. Moita, G. Jelenic, and L. P. R. Lyons, "Enhanced lower-order element formulations for large strains," *Comput. Mech.*, **17**, 62–73 (1995).
10. W. Dettmer and S. Reese, "On the theoretical and numerical modeling of Armstrong–Frederick kinematic hardening in the finite strain regime," *Comput. Meth. Appl. Mech. Eng.*, **193**, 87–116 (2004).
11. A. Dogui and F. Sidoroff, "Kinematic hardening in large strain elastoplastic strain," *Eng. Fract. Mech.*, **21**, No. 4, 685–695 (1985).
12. A. Düster, S. Hartmann, and E. Rank, "p-FEM applied to finite isotropic hyperelastic bodies," *Comput. Meth. Appl. Mech. Eng.*, **192**, No. 47–48, 5147–5166 (2003).
13. M. Ekh and K. Runesson, "Modeling and numerical issues in hyperelasto-plasticity with anisotropy," *Int. J. Solids Struct.*, **38**, No. 52, 9461–9478 (2001).
14. S. Glaser and F. Armero, "On the formulation of enhanced strain finite elements in finite deformations," *Eng. Comput.*, **14**, No. 7, 759–791 (1997).
15. E. M. Gunel and C. Basaran, "Damage characterization in non-isothermal stretching of acrylics. Part I: Theory," *Mech. Mater.*, **43**, No. 12, 979–991 (2011).
16. E. M. Gunel and C. Basaran, "Damage characterization in non-isothermal stretching of acrylics. Part II: Experimental validation," *Mech. Mater.*, **43**, No. 12, 992–1012 (2011).

17. E. Gunel and C. Basaran, "Influence of filler content and interphase properties on large deformation micromechanics of particle filled acrylics," *Mech. Mater.*, **57**, 134–146 (2013).

18. U. Heisserer, S. Hartmann, A. Düster, W. Bier, Z. Yosibash, and E. Rank, "p-FEM for finite deformation powder compaction," *Comput. Meth. Appl. Mech. Eng.*, **197**, No. 6–8, 727–740 (2008).

19. E. Kirchner, S. Reese, and P. Wriggers, "A finite element method for plane stress problems with large elastic and plastic deformations," *Commun. Numer. Meth. Eng.*, **13**, No. 12, 963–976 (1997).

20. S. Klinkel and S. Govindjee, "Using finite strain 3D-material models in beam and shell elements," *Eng. Comput.*, **19**, No. 8, 254–271 (2002).

21. O. Köhler and G. Kuhn, "The Domain-Boundary Element Method (DBEM) for hyperelastic and elastoplastic finite deformation: axisymmetric and 2D/3D problems," *Arch. Appl. Mech.*, **71**, 436–452 (2001).

22. X. Li, C. C. Roth, and D. Mohr, "Machine-learning based temperature-and rate-dependent plasticity model: application to analysis of fracture experiments on DP steel," *Int. J. Plasticity*, **118**, 320–344 (2019).

23. J. Liu, J. Li, G. Dirras, K. Ameyama, F. Cazes, and M. Ota, "A three-dimensional multi-scale polycrystalline plasticity model coupled with damage for pure Ti with harmonic structure design," *Int. J. Plasticity*, **100**, 192–207 (2018).

24. G. Lührs, S. Hartmann, and P. Haupt, "On the numerical treatment of finite deformations in elastoviscoplasticity," *Comput. Meth. Appl. Mech. Eng.*, **144**, Nos. 1–2, 1–21 (1997).

25. A. Menzel, M. Ekh, K. Runesson, and P. Steinmann, "A framework for multiplicative elastoplasticity with kinematic hardening coupled to anisotropic damage," *Int. J. Plasticity*, **21**, No. 3, 397–434 (2005).

26. A. Menzel and P. Steinmann, "On the spatial formulation of anisotropic multiplicative elasto-plasticity," *Comput. Meth. Appl. Mech. Eng.*, **192**, Nos. 31–32, 3431–3470 (2003).

27. S. Narayan and L. Anand, "A large deformation elastic–viscoplastic model for lithium," *Extreme Mech. Lett.*, **24**, 21–29 (2018).

28. R. R. Paccola and H. B. Coda, *AcadView: Software for post-processing in 2D and 3D finite elements*, São Carlos: Escola de Engenharia de São Carlos, Universidade de São Paulo (2005).

29. J. P. Pascon, "Finite element analysis of flexible functionally graded beams with variable Poisson's ratio," *Eng. Comput.*, **33**, No. 8, 2421–2447 (2016).

30. J. P. Pascon and H. B. Coda, "Analysis of elastic functionally graded materials under large displace ments via high-order tetrahedral elements," *Finite Elem. Anal. Des.*, **50**, 33–47 (2012).

31. J. P. Pascon and H. B. Coda, "High-order tetrahedral finite elements applied to large deformation analysis of functionally graded rubber-like materials," *Appl. Math. Model.*, **37**, Nos. 20–21, 8757–8775 (2013).

32. J. P. Pascon and H. B. Coda, "A shell finite element formulation to analyze highly deformable rubber-like materials," *Lat. Am. J. Solids Struct.*, **10**, No. 6, 1177–1209 (2013).

33. J. C. Simo and F. Armero, "Geometrically non-linear enhanced strain mixed methods and the method of incompatible modes," *Int. J. Numer. Meth. Eng.*, **33**, No. 7, 1413–1449 (1992).

34. J. C. Simo, F. Armero, and R. L. Taylor, "Improved versions of assumed enhanced strain tri-linear elements for 3D finite deformation problems," *Comput. Meth. Appl. Mech. Eng.*, **110**, Nos. 3–4, 359–386 (1993).

35. J. C. Simo and M. Ortiz, "A unified approach to finite deformation elastoplastic analysis based on the use of hyperelastic constitutive equations," *Comput. Meth. Appl. Mech. Eng.*, **49**, No. 2, 221–245 (1985).

36. A. Srikanth and N. Zabaras, "An updated Lagrangian finite element sensitivity analysis of large deformations using quadrilateral elements," *Int. J. Numer. Meth. Eng.*, **52**, No. 10, 1131–1163 (2001).

37. L. Stainier and J. Ph. Ponthot, "An improved one-point integration method for large strain elastoplastic analysis," *Comput. Meth. Appl. Mech. Eng.*, **118**, Nos. 1–2, 163–177 (1994).

38. P. Steinmann, P. Betsch P., and E. Stein, "FE plane stress analysis incorporating arbitrary 3D large strain constitutive models," *Eng. Comput.*, **14**, No. 2, 175–201 (1997).

39. B. Svendsen, "A thermodynamic formulation of finite-deformation elastoplasticity with hardening based on the concept of material isomorphism," *Int. J. Plasticity*, **14**, No. 6, 473–488 (1998).

40. H. Swift, "Length changes in metals under torsional overstrain," *Eng.*, **163**, 253–257 (1947).

41. K. Y. Sze, S. J. Zheng, and S. H. Lo, "A stabilized eighteen-node solid element for hyperelastic analysis of shells," *Finite Elem. Anal. Des.*, **40**, No. 3, 319–340 (2004).

42. A. Taghipour, J. Parvizian, S. Heinze, and A. Düster, "p-version finite elements and finite cells for finite strain elastoplastic problems," *PAMM*, **16**, No. 1, 243–244 (2016).

43. A. Taghipour, J. Parvizian, S. Heinze, and A. Düster, "The finite cell method for nearly incompressible finite strain plasticity problems with complex geometries," *Comput. Math. Appl*., **75**, No. 9, 3298–3316 (2018).

44. I. N. Vladimirov, M. P. Pietryga, and S. Reese, "On the modelling of non-linear kinematic hardening at finite strains with application to springback–Comparison of time integration algorithms," *Int. J. Numer. Meth. Eng*., **75**, No. 1, 1–28 (2008).

45. I. N. Vladimirov, M. P. Pietryga, and S. Reese, "Prediction of springback in sheet forming by a new finite strain model with nonlinear kinematic and isotropic hardening," *J. Mater. Process. Technol*., **209**, No. 8, 4062–4075 (2009).

46. E. Voce, "The relationship between stress and strain for homogeneous deformation," *J. Inst. Metals*, **74**, 537–562 (1948).

47. W. Zhao, M. Ries, P. Steinmann, and S. Pfaller, "A viscoelastic-viscoplastic constitutive model for glassy polymers informed by molecular dynamics simulations," *Int. J. of Solids Struct*., **226–227**, 111071 (2021).